

Towards multi-petahertz all-optical electric field sampling

Anton Husakou¹, Nicholas Karpowicz^{2,3},
Vladislav S. Yakovlev^{2,3}, Misha Ivanov¹, Dmitry A. Zimin⁴

¹Max Born Institute for Nonlinear Optics and Short Pulse Spectroscopy,
Berlin, Germany.

²Max-Planck-Institut für Quantenoptik, Garching, Germany.

³Fakultät für Physik, Ludwig-Maximilians-Universität, Garching,
Germany.

⁴Laboratory of Physical Chemistry, ETH Zürich, Zürich, Switzerland.

Abstract

We present an all-optical concept for measuring the electric field of light spanning from infrared to extreme ultraviolet with multi-petahertz detection bandwidth. Our approach employs a heterodyne detection of light produced by a highly nonlinear light-matter interaction gate. We establish a numerical model of a complex spectral response for unambiguous electric field extraction and benchmark it against the experiment. We show that the concept can be applied for measuring wavelengths down to about 60 nm with a high sensitivity and dynamic range of about 40 decibels. This opens up unprecedented perspectives for spatio-temporal electric field-resolved experiments and control of broadband dynamics of matter.

Keywords: Electric field, petahertz, ultrafast

1 Introduction

Upon light-matter interaction, the spatio-temporal evolution of the electric field brings matter into motion. The response of matter evolves in time and space and can be imprinted on the interacting field. By reading out this information, access to underlying physical processes can be obtained. This concept called field-resolved metrology (FRM) has been recently utilized to measure the formation of the optical response from the electron-hole plasma[1, 2], ultrafast magnetism[3], and the light-matter energy

transfer[4] in photoexcited solids. Generally, unlike conventional spectroscopy, FRM allows tracking matter dynamics *during* the light-matter interaction with a sub-cycle temporal resolution and extremely high sensitivity[5, 6]. It was also recently shown that the electric field can potentially be used to encode digital information[7] and serve as a computing gate[8] and memory[9], paving the way towards petahertz (1 PHz = 10^{15} Hz) optoelectronics[10]. For this, knowing the spatio-temporal profile of the broadband field is vital.

Sampling of the electric field of light is challenging and is at the focus of contemporary research[11, 12]. It requires a gating event[13]. In the Auston switch[14] this event is achieved by changing material conductivity; in the attosecond (1 as = 10^{-18} s) streak camera[15] by a single photon ionization; in linear[16] and nonlinear[17, 18] photo-conductive sampling by a photoinjection[19]; in TIPTOE[20–22] by tunneling ionization. Non-optical gates described above exhibit drawbacks: i) the bandwidth rapidly rolls off as the duration of the gate becomes comparable to the half-cycle of the measured frequency. Sampling of 600 nm light already requires an attosecond-scale gate, hence intense ultrashort pulses, complex experimental infrastructure, and highly nonlinear light-matter interaction are required; ii) the non-optical nature prevents using optical cameras despite attempts towards spatial extension[23, 24]; iii) the sensitivity and the dynamic range are far behind all-optical methods where heterodyne detection is utilized[5, 25].

Optical gates are produced by nonlinear light emission. Electro-optic sampling [26–30] and air-biased coherent detection [31, 32] are typical examples. These gates allow accessing the electric field in time[14, 27–29] and space[30] with a very high sensitivity and dynamic range[5, 25]. It has been recently shown that in contrast to non-optical gates, the spectrally resolved measurement of light emerging from nonlinear wave mixing obviates the need for the optical gate to be shorter than the half-cycle of the measured frequency[25]. The spectral responses of such methods are well-understood. However, the low order of nonlinear light-matter interaction limits the detection bandwidth.

To date, both non-optical and all-optical approaches struggle to access frequencies above 1 PHz (~ 300 nm wavelength), curtailing physical processes which can be studied. For instance, the vibrational motion of matter is typically at mid-infrared frequencies, excitonic and plasmonic dynamics[33] are between infrared and ultraviolet, while electronic transitions can be in the domain of extreme ultraviolet or X-ray[34] light. Broader detection bandwidth also implies an enhanced temporal resolution that is crucial for accessing ultrafast sub-femtosecond dynamics.

We present a concept for measuring the electric field of light spanning from infrared to extreme ultraviolet, which overcomes the bandwidth limitation of all state-of-the-art FRM methods. The concept relies on employing highly nonlinear processes such as cascaded nonlinearities (consecutive generation of new spectral components with propagation) as well as Brunel radiation (associated with time-dependent plasma density) [35] and recently observed injection current [36] (provided by the electron displacement during tunneling) as optical gates for sampling of high frequencies.

Our concept combines the advantages of non-optical (temporal confinement) and optical (high sensitivity) gates. We develop a theoretical model that accounts for the

nonlinear propagation of light in the medium, photoexcitation, and plasma dynamics. The model provides an excellent agreement with the experiment. We find that the detection bandwidth of this concept can extend into the multi-petahertz regime. At the same time, the high sensitivity is preserved by the all-optical heterodyne nature of the detection. Our study paves the way for investigations based on broadband electric-field measurement up to extreme ultraviolet.

2 Results

The idea of all-optical FRM is to combine the pulse to be measured (test, with the field $E_T(t)$) with another (sampling, with the field $E_S(t)$) and to induce a nonlinear light-matter interaction (Fig. 1a) in a nonlinear medium (NM). The nonlinearly generated pulse (NP, with the field $E_{NP}(\tau, t)$) is unique for each temporal delay (τ) between pulses and proportional to the electric field of the test pulse at the moment of the gating event. To measure the electric field, the NP from each delay τ is interfered with another "stationary" light called a local oscillator (LO). The LO does not depend on the delay and serves as a reference for the heterodyne detection. We measure intensity $I(\tau, \omega_0)$ of the heterodyne interference between NP and LO at a defined frequency ω_0 and record it for various delays τ . Experimentally the ω_0 is set by the bandpass filter (BP) and the photodiode (PD) response function (more in SI) and in our experiment, it is about 355 nm.

$$I(\tau, \omega_0) \sim |E_{NP}(\tau, \omega_0) + E_{LO}(\omega)|^2 \sim E_{NP}^*(\tau, \omega_0)E_{LO}(\omega_0) + E_{NP}(\tau, \omega_0)E_{LO}^*(\omega_0). \quad (1)$$

In our study, an octave-spanning (450 - 1000 nm), carrier-envelope phase (CEP) stable, sub-3 fs pulse[17] is split into two orthogonally polarized replicas: sampling and test, with a controlled time delay τ between them. After setting the field strength and the CEP of each pulse, the pulses are recombined and co-linearly focused on the nonlinear medium. The test pulse was kept weak while the field strength of the sampling pulse was varied between 0.52 and 1.54 V/Å. We used a z-cut α -quartz crystal of $\sim 12 \mu\text{m}$ thickness as the nonlinear medium. The combination of the nonlinear tensor of the z-cut α -quartz and the wire-grid polarizer allows us to set up the generalized heterodyne optical sampling technique (GHOST)[25] where the second harmonic (SHG) of the sampling pulse serves as LO. The four-wave mixing (FWM) between the sampling and test pulses serves as NP. The GHOST spectral response of the SHG+FWM channel covers only the edges of the test spectrum. This can be intuitively understood as follows. If the fundamental spectrum of the sampling and test pulses is centered at a frequency ω_S then the SHG is at $2\omega_S$. When the SHG is used as a LO, and the FWM as a signal, the heterodyne condition $\omega_S \pm \omega_S \pm \omega_T = 2\omega_S$ can be fulfilled only for $\omega_T = 0$ or $\omega_T = 2\omega_S$, but not for $\omega_T = \omega_S$.

We start with a moderate 0.52 V/Å sampling field strength. This field strength is high enough for 2nd- and 3rd-order nonlinear light-matter interaction, but too weak[4] for efficient higher-order effects such as cascaded processes, Brunel radiation or injection current. The 2nd- and 3rd-order optical nonlinearities arise from anharmonicity[37] of the electron motion (Fig. 1b). Fig. 1c displays the recorded

GHOST trace $I(\tau, \omega_0)$, while Fig. 1d shows the corresponding spectrum. This measurement captures only a small fraction of the test pulse bandwidth consistent with the expected spectral response of the SHG+FWM channel (Fig. 4a) and exemplifies the bandwidth limitation of the conventional GHOST scheme.

We now attempt to overcome this limitation and achieve broadband detection. We increase the sampling field strength to 1.54 V/\AA and repeat the experiment, expecting higher nonlinear processes to become efficient and to contribute to the NP. In stark contrast to the weak-field case, the recorded trace (Fig. 1e) now covers the entire bandwidth of the test pulse (Fig. 1f). We note that this is not possible with conventional SHG+FWM GHOST indicating the key role of higher-order nonlinear processes. We also note an increase in the overall signal by about three orders of magnitude. Equally important, we observe a high dynamic range (ratio of the strongest to the weakest signal) of about 40 decibels. We identify three possible mechanisms. At higher intensities, newly generated frequencies participate in the nonlinear wave mixing during propagation, leading to cascade nonlinear effects (Fig. 1b). At even higher intensities, electrons are excited to the conduction band. Two nonlinear effects are associated with this photoexcitation: injection current[36] and Brunel radiation[35] (Fig. 1b). So far only non-optical gates[17, 38] exploit these highly nonlinear processes. Here we utilize them as optical gates instead, and therefore combine advantages of both approaches, such as temporal confinement and heterodyne detection with high sensitivity.

We repeat the experiment shown in Fig. 1 for various sampling field strengths to investigate the transition from the weak-field regime with a narrowband response towards a strong-field regime with a broadband response and benchmark it against the model (Fig. 2a-d). As we increase the field strength to 0.72, 1.42, and 1.52 V/\AA , we observe a transition from the narrowband to the broadband response which agrees well with our model indicating that it captures most or all of the relevant processes.

To understand the transition to the broadband response, we modeled the nonlinear propagation of light through the medium, accounting for the 2d- and 3d-order nonlinear light-matter interactions, as well as for strong-field processes such as Brunel radiation and injection current (more in Methods). We employ forward-propagation equation[39] without slowly-varying envelope approximation and automatically include cascaded effects of propagation, as well as group velocity dispersion to all orders, linear absorption, and self-steepening. We characterize the sampling and test pulses with FROG[40] and use this data as input for the model.

We now proceed to unravel the underlying physics. The weak-field GHOST spectral response is mainly confined to around 0.65 PHz (Fig. 2a), while the strong-field response covers the entire available spectrum. We evaluate the power-law dependence of the signal at 0.45 PHz and 0.65 PHz versus the field strength of the sampling pulse E_S (Fig. 2e). We first confirm that the integrated signal around 0.65 PHz scales with the sampling field strength to the power of four ($IS \propto E_S^4$). This is expected since the SHG+FWM GHOST requires two photons for LO and two photons for NP from the sampling pulse. Interestingly, for 0.45 PHz two regimes are identified (Fig. 2e): Up to about 1.1 V/\AA the signal scales as the sixth power, attributed to cascaded nonlinearities in the NP arm which require (at least) one more nonlinear interaction during propagation, involving two more photons. Above 1.1 V/\AA , a deviation from the E_S^6 is

observed, related to the onset of Brunel and injection current mechanisms. Our model adequately reproduces both regimes.

As we show later, these mechanisms provide the broadest multi-PHz response since the moment of the photoinjection of charge carriers is strongly confined in time. In contrast to the previous work where the sudden displacement of photoinjected electrons was measured as current[17], here we detect light emitted due to this sudden displacement which effectively converts a non-optical gate into optical. Fig. 2f compares the simulated contributions of light-matter interaction based on 2nd- and 3rd-order nonlinearities only (including cascaded processes), to the contribution of nonperturbative strong-field light-matter interaction based on Brunel and injection current. The simulation indicates that Brunel and injection current mechanisms can be used as optical gates with associated spectral responses, however, under our experimental conditions their contribution is only about 0.3 %. This contribution however strongly depends on the sampling field strength and will be maximized at the fields close to the damage threshold. The field strength in this experiment was about 2.5 times lower than the damage threshold. Furthermore, the photoinjection of charge carriers is mainly confined to the front surface of the medium (more in SI), while the light originating from the perturbative light-matter interaction accumulates across the entire thickness (12 μm of quartz in our experiment). Therefore strong fields and thin media are required to unlock the full potential of this regime.

To further confirm that highly nonlinear processes dominate the spectral response in the strong-field regime, we record GHOST traces as a function of sampling pulse CEP, as shown in Fig. 3d. We expect a strong CEP dependence of the signal due to gating events occurring at the field maxima of the sampling pulse, with the broadest and smoothest response obtained for a CEP of $0, \pi, 2\pi$, etc., corresponding to a single well-pronounced field maximum. Indeed, both experimentally and numerically, we see a broad response at CEP around 0 and π , with a dip in the spectral profile of the signal for CEP around $\pi/2$ (Fig. 3c,d). Thus, in contrast to the weak-field regime, the spectral response is clearly sensitive to the CEP of the sampling pulse, with a π -periodicity which is consistent with our model.

Finally, we benchmark our model against the experiment in the strong ($E_S = 1.54$ V/ \AA) field regime directly in the time domain (Fig. 3a). The model accurately reproduces the experiment in both, the time and frequency domains (Fig. 3b,c), highlighting precision and accuracy of the electric field measurement.

3 Discussion

For the test pulse much weaker than the sampling pulse, the signal after the nonlinear medium is linearly related to the test electric field:

$$E_{\text{NP}}(\tau, t) = \int_{-\infty}^{\infty} G(t, \tau') E_{\text{T}}(\tau' - \tau) d\tau', \quad (2)$$

where $G(t, \tau')$ is the Green's function. After transformations, one obtains the Fourier transform of $I(\tau, \omega_0)$ with respect to τ :

$$I(\omega, \omega_0) = -[G^*(z, \omega_0, \omega)E_I(z, \omega_0) + G(z, \omega_0, \omega)E_I^*(z, \omega_0)]E_T^*(\omega) = R(z, \omega)E_t^*(\omega), \quad (3)$$

where a complex-valued response function $R(z, \omega)$ connects the measured signal with the test electric field.

At the first stage of propagation, new frequencies are generated and participate in the nonlinear mixing at a later propagation stage. While we cannot switch these cascaded processes on and off experimentally, it can be done numerically (Fig. 4a,b) by setting the number of z steps to 1. The broadening of the response and appearance of the signal between 0.35 PHz and 0.5 PHz is clearly connected to the cascaded mechanism, since without it the spectral shape is similar to that of the low-intensity case. Several nonlinearities that can lead to cascaded spectral broadening are self-phase modulation, self-steepening, third harmonic generation, four-wave mixing, etc. In the framework of the slowly varying envelope approximation, it would be easy to separate the above contributions since they correspond to different terms. However, in the case of very short pulses, such approximation cannot be used, and the nonlinear polarization $P_{NL}(t) = \epsilon_0 \chi_3 E^3(t)$ cannot be trivially split into different mechanisms. Nevertheless, we have developed an approach (more in SI) which allows separating frequency mixing with the identical signs (IS): $\omega = +\omega_1 + \omega_2 + \omega_3$, and with different signs (DS): $\omega = +\omega_1 + \omega_2 - \omega_3$. The IS term incorporates the sum-frequency mixing of three photons, such as the mixing of two sampling photons and one test photon ($\omega = +\omega_S + \omega_s + S + \omega_T$), as well as third harmonic generation. The DS term describes several parametric and mixing processes: ($\omega = +\omega_S - \omega_s + \omega_T$, $\omega = +\omega_S + \omega_s - \omega_T$, $\omega = +\omega_S - \omega_s - \omega_T$, etc.) and includes further contributions such as self-phase modulation. In Fig. 4c,d we show the role of the IS and DS terms in the response function $R(\omega)$ for the low- and high-intensity cases. For low-intensity case, the low-frequency term consists of both IS and DS contributions while the high-frequency peak is generated solely by the DS term. For higher intensity, it is the DS term that provides spectral broadening of the response function and broadband detection. For even higher field strengths, in addition to cascaded processes, the photoinjection-related mechanisms (Brunel radiation and injection current) begin to play a comparable role.

We now turn our attention to exploring the limits and perspectives of this concept. We evaluate a simulated response function $R(\omega)$ across the entire infrared to extreme ultraviolet spectrum (0 - 5 PHz) under realistic experimental conditions. Since the Brunel radiation and injection current are mainly confined to the surface (more in SI), it is beneficial to use thin nm-scale medium, which additionally minimize absorption of light above the band gap. Equally important, high-order nonlinearities are enabled at high field strengths, therefore we consider a SiO_2 (Fig. 5a,c) and diamond (Fig. 5b,d) that can sustain high intensity. These samples also provide high 3rd-order nonlinearity ($3 \times 10^{-20} \text{ cm}^2/\text{W}$ [41] and $10 \times 10^{-20} \text{ cm}^2/\text{W}$ [42], correspondingly) necessary for cascaded processes, large bandgaps (9 eV[43] and 5.5 eV [44], correspondingly) and can be experimentally made as a free-standing films of 20 nm thickness[45, 46]. We however note that not only a solid medium but also gas or liquid, can serve this purpose. The simulation (Fig. 5a,b) clearly indicates that higher-order nonlinear processes

enable the extension of the detection bandwidth towards the multi-PHz range (up to about 5 PHz, 60 nm wavelength) in both samples. Interestingly we find that in case of diamond (Fig. 5a), the Brunel and injection current processes dominate while in the SiO₂ (Fig. 5b), the cascaded nonlinearities contribute the most. This can be connected to the smaller bandgap of the diamond, which expedites the photoexcitation and thus enhances Brunel and injection current mechanisms. With photoionization-related and cascaded effects switched off (Fig. 5a,b, orange curves), we predict a response function with a few separate peaks expected for low-intensity GHOST. This again highlights the important role of the Brunel radiation and injection current in achieving a continuous broadband response.

For direct measurement of the electric field, the absolute spectral phase response is of a key importance (Fig. 5c,d). The spectral phase response across the entire spectrum up to 5 PHz is relatively flat, which is favorable from the practical perspective. We attribute this to the thin medium considered in the simulation.

Overall our model predicts that the concept enables measurements of the electric field of photons across an extremely broad spectral range including the extreme ultraviolet.

4 Conclusion

We have introduced a novel all-optical concept for measuring the electric field of light with an extremely broad multi-petahertz bandwidth. Our approach employs optical gates for heterodyne detection similar to conventional electro-optic sampling or GHOST schemes. By contrast, we employ highly nonlinear processes such as cascaded nonlinearities, Brunel radiation, and injection current. We show that light emitted by strong-field processes that are confined in time can be used as optical gates. This confinement provides a broad spectral response sufficient to sample electric fields across the infrared to extreme ultraviolet range. The heterodyne detection preserves a high sensitivity which is typical for all-optical methods.

We have developed a numerical model and benchmarked it against the experiment measuring sub-3 fs state-of-the-art optical pulses with octave-spanning bandwidth. Both experimentally and theoretically, we observe a clear transition from the narrowband response in the weak-field regime to the extremely broadband response in the strong-field regime. We confirm that the broadening of the spectral response is achieved by involving highly nonlinear processes such as cascaded nonlinearities, Brunel radiation and injection current.

The multi-petahertz spectral response enables electric field-resolved studies across the broad spectrum spanning from infrared to extreme-ultraviolet, including high-harmonic generation, or charge transfer during chemical reactions. Furthermore, the all-optical nature can be utilized for future imaging applications.

5 Methods

For numerical simulations, we use the unidirectional pulse propagation equation without slowly varying envelope approximation, including the following effects: Kerr nonlinearity (which includes self-phase modulation, cross-phase modulation, four-wave

mixing, third harmonic generation, self-steepening, etc.), second-harmonic generation for the emission of the local oscillator, group velocity dispersion, linear losses, Brunel radiation emission, and injection current due to photoexcitation displacement. This equation is solved for the sampling pulse. For the local oscillator, as well as for the NP pulse as a function of the delay, we solve the linearized equation since the energy of both of these pulses is lower than that of the sampling pulse. A detailed description of the model is given in the following sections.

5.1 Sampling pulse propagation

The following equation is used to model the sampling pulse propagation[39]:

$$\begin{aligned} \frac{\partial E_S(z, \omega)}{\partial z} = & -i \left(\frac{[\sqrt{\varepsilon(\omega)} - n_g]\omega}{c} - \beta(\omega_0) \right) E_S(z, \omega) \\ & - \frac{i\omega}{2c\sqrt{\varepsilon(\omega)}} P_{NL}(z, \omega), \end{aligned} \quad (4)$$

where $E_S(z, \omega) = \hat{F}E_S(z, t) = \int_{-\infty}^{\infty} E_S(z, t) \exp(-i\omega t) dt$ is the Fourier transform \hat{F} of the electric field $E_S(z, t)$, z is the propagation coordinate, $\varepsilon(\omega)$ is the linear dielectric permittivity, n_g is the group refractive index, ω_S is a characteristic frequency of the pulse spectrum, $\beta(\omega) = \sqrt{\varepsilon(\omega)}\omega/c$, and $P_{NL}(z, \omega)$ is the Fourier transform of the nonlinear part of the polarization. This equation is a forward-propagation equation, i.e. the backward-propagating wave in the sample is neglected. This assumption is justified as long as the nonlinear modification of the dielectric function, e.g. by the plasma contribution, is small. This condition holds as long as we are not approaching the metallization regime of the sample by the free carriers, which is usually accompanied by damage. We also neglect the transverse dynamics (self-focusing, diffraction, etc.), since the beam is sufficiently wide (several tens of micrometers), and the propagation length is no longer than 12 micrometers. The slowly varying envelope approximation is not used, and $E_S(z, t)$ represents the real field and includes the carrier oscillations. This approach yields a unified treatment for a sampling pulse with arbitrary spectral content, which is critical for extremely broad spectra considered here. The dielectric function $\varepsilon(\omega)$ was calculated using the standard Sellmeyer equation and included loss for the frequencies above the bandgap of the quartz. For very high frequencies above 2 PHz, The expressions used are less reliable, however, this does not undermine the accuracy of the model, since in the case of multi-PHz sampling we have considered a 20 nm thin sample which does not cause any significant linear loss. The group refractive index n_g was chosen so that the pulse does not shift in the time domain during the propagation.

The nonlinear polarization includes the standard term originating from the third-order susceptibility $P_{NL, Kerr}(z, t) = \varepsilon_0 \chi_3 E_S(z, t)^3$, as well as plasma-related terms which describe Brunel radiation and the injection current. Here we neglect higher-order perturbative nonlinearities (χ_5, χ_7 , etc.). The reliable characterization of these nonlinearities is not currently available, and in many cases, they are associated with

photoionization, which is included in our model. We also do not consider harmonics generated by the three-step mechanism in the solid state (photoionization to the conduction zone, acceleration of almost-free carriers, followed by the recombination), since it is usually characterized by the emission of high-energy photons with energies above bandgap, which are not relevant for the present study.

The above contributions are determined by the average electron position $\langle d \rangle(z, t)$ of the electron from the equilibrium position in the parent "molecule". Here, by a "molecule", we denote an atom or a group of atoms of the solid-state which provides a single ionization event. Such treatment is itself an approximation, which is justified by the large bandgap of the quartz and the corresponding strong localization of the electrons. Furthermore, it is determined by the relative ionization $\rho(z, t)$, which is the ratio of the conduction-band electron density to the density of "molecules":

$$P_{\text{plasma}}(z, \omega) = -N_{\text{mol}} e \hat{F}[\langle d \rangle(z, t) \rho(z, t)], \quad (5)$$

here N_{mol} is the concentration of the molecules and $e = 1.6 \times 10^{-19}$ is the electron charge. The dynamics of the $\langle d \rangle(z, t) \rho(z, t)$ is given by

$$\frac{\partial(\langle d \rangle(z, t) \rho(z, t))}{\partial t} = \langle v \rangle(z, t) + x_0 \Gamma(t), \quad (6)$$

where $\langle v \rangle$ is the average electron velocity and $x_0(z, t) \simeq -I_p / e E_S(z, t)$ is the initial displacement of the electron after the ionization event[36], where I_p is the bandgap. The ionization rate $\Gamma(t)$ was described by Ivanov-Yudin formalism[47]. Here we use the expression for x_0 provided by the tunneling exit in an isolated atom, which is again justified by the large bandgap. The first term in this expression describes the Brunel radiation, while the second term describes the injection current, or, equivalently, the energy loss of the pulse due to photoionization. The time evolution of the $\langle v \rangle(z, t) \rho(z, t)$ is given by the second Newton's law as

$$\frac{\partial(\langle v \rangle(z, t) \rho(z, t))}{\partial t} = -\frac{e E_S(z, t)}{m_e} \rho - \nu \langle v \rangle(z, t) \rho(z, t), \quad (7)$$

where m_e is the effective electron mass and ν is the electron collision rate. Here we disregard the initial velocity of the electron after the ionization, as well as the anisotropy of the effective mass as well as its dependence on the position in the Brillouin zone.

5.2 Propagation of the test, local oscillator, and NP pulses

The same approach as above was chosen to simulate the propagation of the test pulse $E_T(z, t)$, local oscillator pulse $E_{LO}(z, t)$, and NP pulse $E_{NP}(z, t)$. In the presence of these pulses, in principle, the expressions for the nonlinear polarization should include all three pulses, as they will cross-influence each other by means of these nonlinear terms. However, here we utilize the fact that the test, LO, and NP are much weaker than the sampling pulse. Therefore we neglect the influence of these pulses on the sampling pulse propagation. In addition, in the propagation equation for the test, LO and NP, we include only the lowest-order terms with respect to the corresponding field. These terms for the test, LO and NP pulses are

$$P_{\text{NL,T,Kerr}}(z, t) = 3\epsilon_0\chi_3^{\text{T}}E_{\text{S}}(z, t)^2E_{\text{T}}(z, t), \quad (8)$$

$$P_{\text{NL,LO,SHG}}(z, t) = 2\epsilon_0\chi_2E_{\text{S}}^2(z, t), \quad (9)$$

and

$$P_{\text{NL,NP,Kerr}}(z, t) = 3\epsilon_0\chi_3^{\text{NP}}E_{\text{S}}(z, t)^2E_{\text{T}}(z, t), \quad (10)$$

whereby we neglect the third-order nonlinearity for the local oscillator pulse since the corresponding term is smaller than the second-order term, and χ_3^{T} and χ_3^{NP} are the components of the third-order susceptibility tensor corresponding to the polarization of the test and NP pulses.

For the plasma-related terms, we use the plasma density $\rho(z, t)$ as generated by the strong sampling pulse, since the modifications by the test pulse, LO, and NP to the plasma density are small. However, we rigorously take into account the *dynamics* of the plasma as induced by the test pulse and its influence on the test pulse. To do that, we trace the dynamics of $\langle d_{\text{T}} \rangle(z, t)$ and $\langle v_{\text{T}} \rangle(z, t)$ by the equations corresponding to the Eq. (6) and (7) in the previous section of the Supplementary Materials. When doing this, we keep only the terms that are lowest-order in $E_{\text{T}}(z, t)$ as explained above. For injection current, this is achieved by using

$$x_{0,\text{T}}(z, t) = -\frac{I_{\text{p}}E_{\text{T}}(z, t)}{eE_{\text{S}}^2(z, t)}. \quad (11)$$

For the Brunel radiation, this is achieved by substituting $E_{\text{S}}(z, t)$ in Eq. (4) by $E_{\text{T}}(z, t)$.

5.3 Measured signal and response function

The measured signal is determined by the LO and NP pulses. Note that only the latter depends on the delay τ . The measured time-dependent interference intensity $I(\tau, \omega)$ depends on τ and frequency ω , and is given by

$$I(\tau, \omega) = |E_{\text{NP}}(\tau, \omega) + E_{\text{LO}}(\omega)|^2 = E_{\text{NP}}^*(\tau, \omega)E_{\text{LO}}(\omega) + E_{\text{NP}}(\tau, \omega)E_{\text{LO}}^*(\omega), \quad (12)$$

whereby we keep only the terms linear in $E_{\text{NP}}(\tau, \omega)$, and all fields are considered at the output of the sample $z = L$.

The NP pulse after the propagation is related to the test pulse by a linear relation involving the green function $G(t, \tau)$ by the following equation:

$$E_{\text{S}}(\tau, t) = \int_{-\infty}^{\infty} G(t, \tau')E_{\text{t}}(\tau' - \tau)d\tau', \quad (13)$$

where $E_{\text{t}}(\tau' - \tau)$ is the input test pulse shifted by τ .

After transformations, for a fixed frequency ω_0 at which the heterodyne signal is measured,

$$I(\omega, \omega_0) = -[G^*(\omega_0, \omega)E_{LO}(\omega_0) + G(\omega_0, \omega)E_{LO}^*(\omega_0)]E_T^*(\omega). \quad (14)$$

Note that the test pulse spectrum appears as a conjugate, which is relevant for the determination of phases. The expression in the square brackets defines the spectral response $R(\omega)$ in terms of the propagation Green function $G(t, \tau')$ and the local oscillator field $E_L(\omega_0)$.

This equation connects the experimentally measured quantity $I(\tau, \omega_0)$ to the spectrum of the pulse $E_T(\omega)$ to be characterized, with the frequency-dependent proportionality factor $-[G^*(\omega_0, \omega)E_L(\omega_0) + G(\omega_0, \omega)E_L^*(\omega_0)]$ which we denote as response function. Note that in a practical situation, the proportionality factor is also influenced by the frequency-dependent detection efficiency, which was taken into account accordingly.

5.4 Experimental methods

The laser beamline used for the experiments (more in SI) comprises a Ti:Sa oscillator (Rainbow 2, Spectra Physics), followed by chirped pulse amplification to 1 mJ pulse energy at 3 kHz repetition rate, further spectral broadening in a hollow-core fiber and a chirped mirror compressor. The experimental data acquisition (more in SI) was performed with a dual-phase lock-in amplifier (SR-830, Stanford Research Systems) and with a grating spectrometer (Ocean Optics).

Supplementary information.

Acknowledgements. The authors thank Ferenc Krausz for the experimental infrastructure.

Funding. This study is supported by the postdoctoral fellowship of the Swiss National Science Foundation (D.A.Z.).

Author contributions. Conceptualization: D.A.Z. Methodology: D.A.Z., A.H. Experiments: D.A.Z. Theory: A.H., D.A.Z., N.K., V.S.Y., M.I. Visualization: D.A.Z. Supervision: D.A.Z. Writing—original draft: D.A.Z., A. H. Writing—review & editing: D.A.Z., A.H., V.S.Y., N.K., M.I.

Competing interests. The authors declare that they have no competing interests.

Data availability. The datasets generated during and/or analyzed during the current study are available from the corresponding author upon reasonable request.

Corresponding author. Dmitry A. Zimin, email: d.a.zimin@gmail.com

Main figure legends

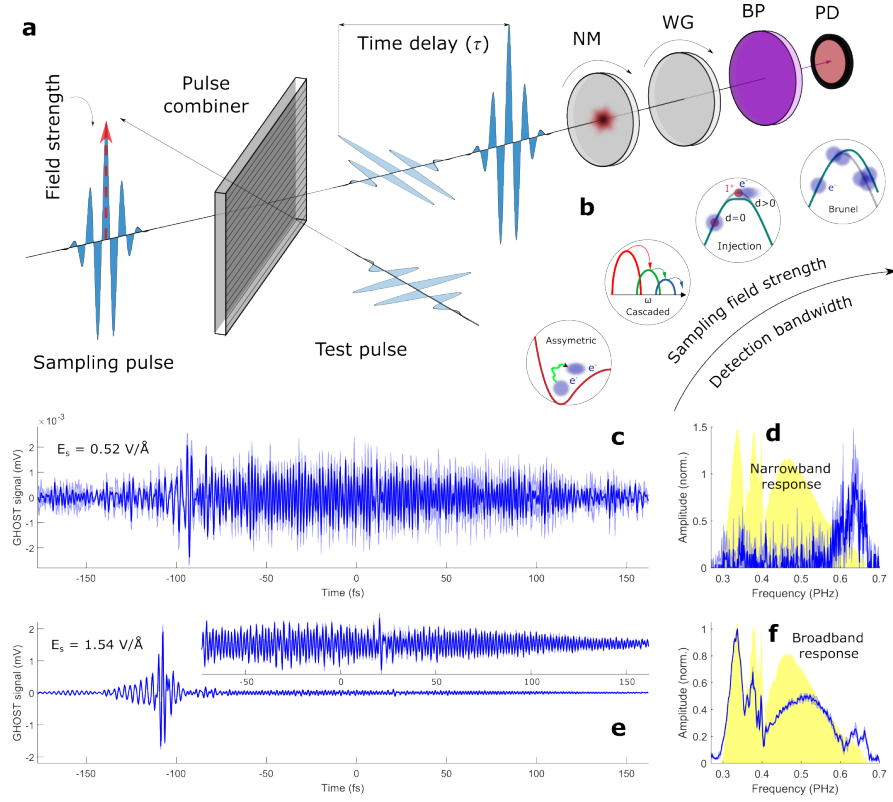


Fig. 1 Summary of the study. **a**, Schematic of the experiment in which two cross-polarized pulses, sampling and test, are recombined with a pulse combiner and focused on a nonlinear medium (NM). The test pulse is kept weak, while the field strength of the sampling pulse varies from 0.52 to 1.54 V/Å. The medium produces a local oscillator (LO) and a nonlinearly-generated pulse (NP) that are guided to a photodiode (PD) for the heterodyne detection of the interference intensity. The wire-grid polarizer (WG) is used to project cross-polarized NP and LO onto one plane. The bandpass filter (BP) is used to select an interference frequency on the photodiode. **b**, Schematic of the concept. As the sampling field strength is increased, more nonlinear processes become accessible, which leads to a broadening of the spectral response. **c**, Measured photodiode signal at various time delays (τ) between two pulses in the weak-field regime. **e**, Measured photodiode signal as a function of time delay (τ) between two pulses in the strong-field regime. **d, f**, Spectrum of the measured signals in **c, e** obtained by a Fourier transformation. The yellow area corresponds to a test pulse spectrum measured with a grating spectrometer.

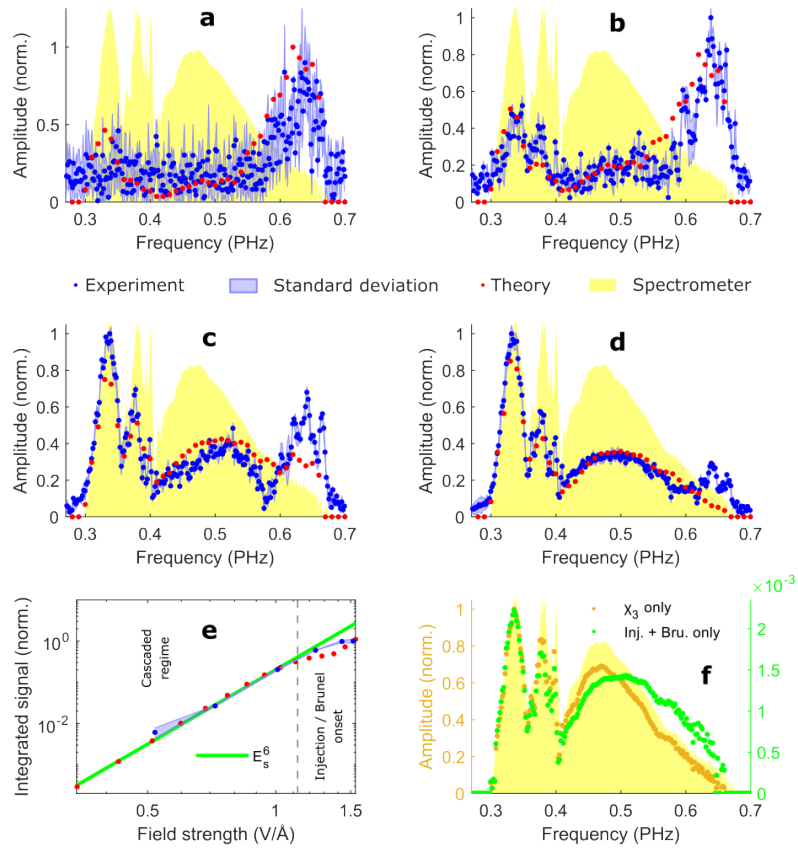


Fig. 2 Transition from the narrowband to the broadband regime. a,b,c,d, Measured and simulated GHOST spectra for the sampling pulse field strengths of 0.52, 1.01, 1.27, and 1.54 V/Å, correspondingly. The yellow shaded area indicates the spectrum of the test pulse, and the shaded blue area denotes the standard deviation. e, Measured and simulated scaling of the integrated signal around 0.45 PHz as a function of the sampling pulse field strength. f, the role of the third-order optical nonlinearity, injection current, and Brunel radiation in the total signal for 1.54 V/Å sampling field strength.

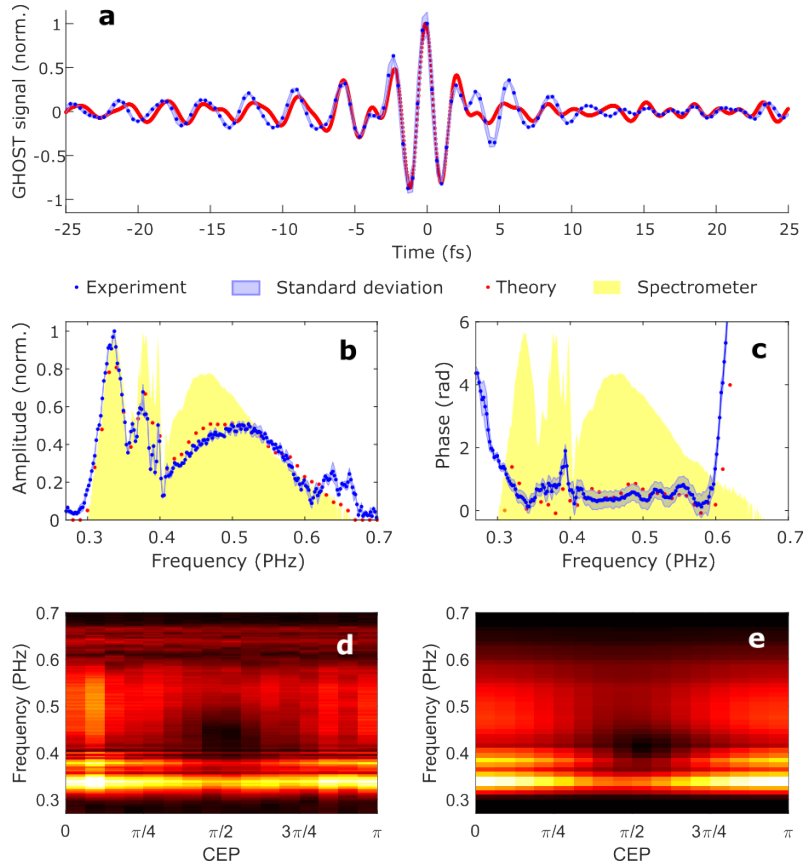


Fig. 3 Benchmarking of the experiment against the model. **a**, the experimental (blue dots) and numerical (red dots) temporal profiles of the GHOST signal for the sampling pulse field of 1.54 V/Å. **b** and **c**, amplitudes and phases of the GHOST spectrum, correspondingly. The experimental (blue dots) and numerical (red dots) amplitudes and phases are shown, together with the yellow shaded area which indicates the spectrum of the test pulse. The shaded blue area denotes the standard deviation. **d**, the measured dependence of the GHOST spectrum on the CEP of the sampling pulse. **e**, the simulated dependence of the GHOST spectrum on the CEP of the sampling pulse.

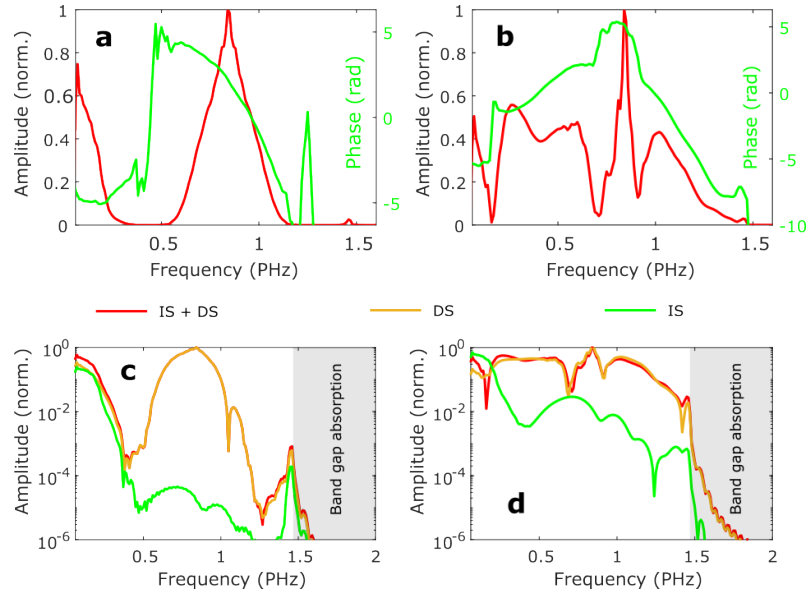


Fig. 4 Disentangling cascaded contributions. **a** and **b**, the spectra (red curves) and the spectral phases (green curves) of the simulated GHOST signal with cascaded processes switched off (**a**) and on (**b**). The field strength of the sampling pulse is 1.54 V/\AA . **c** and **d**, the simulated GHOST spectra with both IS and DS third-order optical processes included (red curves), only DS processes included (orange curves), and only IS processes included (green curves).

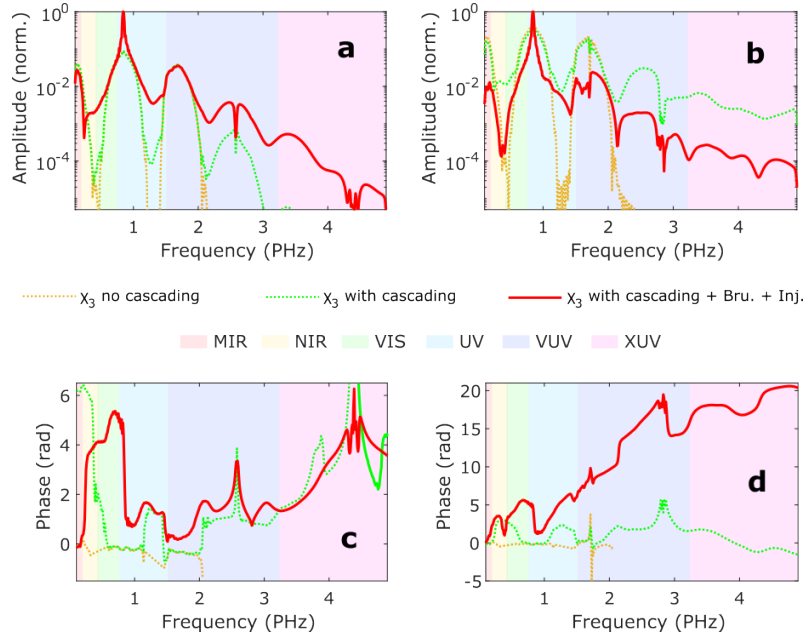


Fig. 5 Perspectives of multi-PHz metrology. **a**, the simulated response function for the thin 20-nm diamond sample with the sampling field strength of 5 V/\AA . The orange curve indicates the spectrum when only third-order nonlinear processes without cascading are included, the green curve shows the spectrum when third-order nonlinear processes with cascading are included, and the red curve represents the case when third-order nonlinearity, Brunel radiation, and injection current are fully included. **b**, the simulated response function for the thin 20-nm SiO_2 sample with sampling field strength of 4 V/\AA . The meaning of the colors is the same as in **a**. **c** and **d**, phases of the response function for the cases shown in **a** and **b**, correspondingly. The meaning of the colors is the same as in **a,b**.

References

- [1] Zimin, D. A. *et al.* Dynamic optical response of solids following 1-fs-scale photoinjection. *Nature* **618**, 276–280 (2023). URL <https://doi.org/10.1038/s41586-023-05986-w>.
- [2] Huber, R. *et al.* How many-particle interactions develop after ultrafast excitation of an electron–hole plasma. *Nature* **414**, 286–289 (2001). URL <https://doi.org/10.1038/35104522>.
- [3] Siegrist, F. *et al.* Light-wave dynamic control of magnetism. *Nature* **571**, 240–244 (2019). URL <http://dx.doi.org/10.1038/s41586-019-1333-x>.
- [4] Sommer, A. *et al.* Attosecond nonlinear polarization and light–matter energy transfer in solids. *Nature* **534**, 86–90 (2016). URL <https://doi.org/10.1038/nature17650>.
- [5] Riek, C. *et al.* Direct sampling of electric-field vacuum fluctuations. *Science* **350**, 420–423 (2015). URL <https://www.science.org/doi/abs/10.1126/science.aac9788>.
- [6] Pupeza, I. *et al.* Field-resolved infrared spectroscopy of biological systems. *Nature* **577**, 52–59 (2020). URL <http://dx.doi.org/10.1038/s41586-019-1850-7>.
- [7] Hui, D. *et al.* Ultrafast optical switching and data encoding on synthesized light fields. *Science Advances* **9**, eadf1015 (2023). URL <https://www.science.org/doi/abs/10.1126/sciadv.adf1015>.
- [8] Boolakee, T. *et al.* Light-field control of real and virtual charge carriers. *Nature* **605**, 251–255 (2022). URL <https://doi.org/10.1038/s41586-022-04565-9>.
- [9] Lee, J. D., Kim, Y. & Kim, C.-M. Model for petahertz optical memory based on a manipulation of the optical-field-induced current in dielectrics. *New Journal of Physics* **20**, 093029 (2018). URL <http://dx.doi.org/10.1088/1367-2630/aae100>.
- [10] Ossiander, M. *et al.* The speed limit of optoelectronics. *Nature Communications* **13** (2022). URL <http://dx.doi.org/10.1038/s41467-022-29252-1>.
- [11] Heide, C., Keathley, P. D. & Kling, M. F. Petahertz electronics. *Nature Reviews Physics* (2024). URL <http://dx.doi.org/10.1038/s42254-024-00764-7>.
- [12] Herbst, A. *et al.* Recent advances in petahertz electric field sampling. *Journal of Physics B: Atomic, Molecular and Optical Physics* **55**, 172001 (2022). URL <http://dx.doi.org/10.1088/1361-6455/ac8032>.
- [13] Agarwal, M., Scrinzi, A., Krausz, F. & Yakovlev, V. S. Theory of nonlinear photoconductive sampling in atomic gases. *Annalen der Physik* **535** (2023). URL <http://dx.doi.org/10.1002/andp.202300322>.

- [14] Auston, D. H., Johnson, A. M., Smith, P. R. & Bean, J. C. Picosecond optoelectronic detection, sampling, and correlation measurements in amorphous semiconductors. *Applied Physics Letters* **37**, 371–373 (1980). URL <https://doi.org/10.1063/1.91947>.
- [15] Kienberger, R. *et al.* Atomic transient recorder. *Nature* **427**, 817–821 (2004). URL <https://doi.org/10.1038/nature02277>.
- [16] Altwajjry, N. *et al.* Broadband photoconductive sampling in gallium phosphide. *Advanced Optical Materials* **11**, 2202994 (2023). URL <https://onlinelibrary.wiley.com/doi/abs/10.1002/adom.202202994>.
- [17] Sederberg, S. *et al.* Attosecond optoelectronic field measurement in solids. *Nature Communications* **11**, 430 (2020). URL <https://doi.org/10.1038/s41467-019-14268-x>.
- [18] Zimin, D. *et al.* Petahertz-scale nonlinear photoconductive sampling in air. *Optica* **8**, 586 (2021). URL <http://dx.doi.org/10.1364/OPTICA.411434>.
- [19] Schötz, J. *et al.* The emergence of macroscopic currents in photoconductive sampling of optical fields. *Nature Communications* **13** (2022). URL <http://dx.doi.org/10.1038/s41467-022-28412-7>.
- [20] Cho, W., Shin, J.-u. & Kim, K. T. Reconstruction algorithm for tunneling ionization with a perturbation for the time-domain observation of an electric field. *Scientific Reports* **11**, 13014 (2021). URL <https://doi.org/10.1038/s41598-021-92454-y>.
- [21] Kubullek, M. *et al.* Single-shot carrier–envelope-phase measurement in ambient air. *Optica* **7**, 35 (2020). URL <http://dx.doi.org/10.1364/OPTICA.7.000035>.
- [22] Bionta, M. R. *et al.* Publisher correction: On-chip sampling of optical fields with attosecond resolution. *Nature Photonics* **15**, 787–787 (2021). URL <http://dx.doi.org/10.1038/s41566-021-00821-y>.
- [23] Blöchl, J. *et al.* Spatiotemporal sampling of near-petahertz vortex fields. *Optica* **9**, 755–761 (2022). URL <https://opg.optica.org/optica/abstract.cfm?URI=optica-9-7-755>.
- [24] Liu, Y. *et al.* Field-resolved space–time characterization of few-cycle structured light pulses. *Optica* **11**, 846–851 (2024). URL <https://opg.optica.org/optica/abstract.cfm?URI=optica-11-6-846>.
- [25] Zimin, D. A., Yakovlev, V. S. & Karpowicz, N. Ultra-broadband all-optical sampling of optical waveforms. *Science Advances* **8**, eade1029 (2022). URL <https://www.science.org/doi/abs/10.1126/sciadv.ade1029>.

- [26] Valdmanis, J. A., Mourou, G. & Gabel, C. W. Picosecond electro-optic sampling system. *Applied Physics Letters* **41**, 211–212 (1982). URL <https://api.semanticscholar.org/CorpusID:121640774>.
- [27] Keiber, S. *et al.* Electro-optic sampling of near-infrared waveforms. *Nature Photonics* **10**, 159–162 (2016). URL <https://doi.org/10.1038/nphoton.2015.269>.
- [28] Ridente, E. *et al.* Electro-optic characterization of synthesized infrared-visible light fields. *Nature Communications* **13**, 1111 (2022). URL <https://doi.org/10.1038/s41467-022-28699-6>.
- [29] Sulzer, P. *et al.* Determination of the electric field and its hilbert transform in femtosecond electro-optic sampling. *Phys. Rev. A* **101**, 033821 (2020). URL <https://link.aps.org/doi/10.1103/PhysRevA.101.033821>.
- [30] Mamaikin, M., Ridente, E., Krausz, F. & Karpowicz, N. Spatiotemporal electric-field characterization of synthesized light transients. *Optica* **11**, 88–93 (2024). URL <https://opg.optica.org/optica/abstract.cfm?URI=optica-11-1-88>.
- [31] Karpowicz, N. *et al.* Coherent heterodyne time-domain spectrometry covering the entire “terahertz gap”. *Applied Physics Letters* **92**, 011131 (2008). URL <https://doi.org/10.1063/1.2828709>.
- [32] Dai, J., Xie, X. & Zhang, X.-C. Detection of broadband terahertz waves with a laser-induced plasma in gases. *Phys. Rev. Lett.* **97**, 103903 (2006). URL <https://link.aps.org/doi/10.1103/PhysRevLett.97.103903>.
- [33] Zimin, D. A. *et al.* Electric-field-resolved detection of localized surface plasmons at petahertz-scale frequencies (2023). URL <https://arxiv.org/abs/2312.11727>.
- [34] Kiryukhin, V. *et al.* An x-ray-induced insulator–metal transition in a magnetoresistive manganite. *Nature* **386**, 813–815 (1997). URL <http://dx.doi.org/10.1038/386813a0>.
- [35] Brunel, F. Harmonic generation due to plasma effects in a gas undergoing multiphoton ionization in the high-intensity limit. *J. Opt. Soc. Am. B* **7**, 521–526 (1990). URL <https://opg.optica.org/josab/abstract.cfm?URI=josab-7-4-521>.
- [36] Jürgens, P. *et al.* Characterization of laser-induced ionization dynamics in solid dielectrics. *ACS Photonics* **9**, 233–240 (2022). URL <https://doi.org/10.1021/acsp Photonics.1c01417>.
- [37] Hora, H. *Y. R. Shen, The Principles of Nonlinear Optics, John Wiley and Sons, New York, 1984, 576 pages.* Vol. 4 (1986).

- [38] Park, S. B. *et al.* Direct sampling of a light wave in air. *Optica* **5**, 402–408 (2018). URL <https://opg.optica.org/optica/abstract.cfm?URI=optica-5-4-402>.
- [39] Husakou, A. V. & Herrmann, J. Supercontinuum generation of higher-order solitons by fission in photonic crystal fibers. *Phys. Rev. Lett.* **87**, 203901 (2001). URL <https://link.aps.org/doi/10.1103/PhysRevLett.87.203901>.
- [40] Stibenz, G. *et al.* Advanced methods for the characterization of few-cycle light pulses: a comparison. *Applied Physics B* **83**, 511–519 (2006). URL <https://doi.org/10.1007/s00340-006-2190-5>.
- [41] Milam, D. Review and assessment of measured values of the nonlinear refractive-index coefficient of fused silica. *Appl. Opt.* **37**, 546–550 (1998). URL <https://opg.optica.org/ao/abstract.cfm?URI=ao-37-3-546>.
- [42] Almeida, J. M. P. *et al.* Nonlinear optical spectrum of diamond at femtosecond regime. *Scientific Reports* **7**, 14320 (2017). URL <https://doi.org/10.1038/s41598-017-14748-4>.
- [43] Moore, L. A. & Smith, C. M. Fused silica as an optical material. *Opt. Mater. Express* **12**, 3043–3059 (2022). URL <https://opg.optica.org/ome/abstract.cfm?URI=ome-12-8-3043>.
- [44] Wort, C. J. & Balmer, R. S. Diamond as an electronic material. *Materials Today* **11**, 22–28 (2008). URL <https://www.sciencedirect.com/science/article/pii/S1369702107703498>.
- [45] URL <https://www.emsdiasum.com/sio2-tem-window8-50%C2%B5m-sq-1-50x100%C2%B5m-20nm>.
- [46] URL <https://www.diamond-materials.com/unsere-produkte/scheiben-schichten-folien/folien-und-membranen/>.
- [47] Yudin, G. L. & Ivanov, M. Y. Nonadiabatic tunnel ionization: Looking inside a laser cycle. *Phys. Rev. A* **64**, 013409 (2001). URL <https://link.aps.org/doi/10.1103/PhysRevA.64.013409>.

Supplementary materials for towards multi-petahertz all-optical electric field sampling

Anton Husakou¹, Nicholas Karpowicz^{2,3},
Vladislav S. Yakovlev^{2,3}, Misha Ivanov¹, Dmitry A. Zimin⁴

¹Max Born Institute for Nonlinear Optics and Short Pulse Spectroscopy,
Berlin, Germany.

²Max-Planck-Institut für Quantenoptik, Garching, Germany.

³Fakultät für Physik, Ludwig-Maximilians-Universität, Garching,
Germany.

⁴Laboratory of Physical Chemistry, ETH Zurich, Zürich, Switzerland.

1 Evolution of the Green function

The Green function is a function of the propagation coordinate and is explicitly denoted by $G(z, t, \tau')$. Its propagation equation is given by

$$\frac{\partial G(z, \omega_0, \omega)}{\partial z} = i\beta(\omega_0)G(z, \omega_0, \omega) + P(z, \omega_0), \quad (1)$$

where

$$P(z, t) = \alpha(z, t)G(z, t, \tau') + \frac{[\partial\beta(z, t)G(z, t, \tau')]}{\partial t} + \int_{-\infty}^t \gamma(z, \tau'')G(z, \tau'', \tau')d\tau'' \quad (2)$$

Note that the propagation equation for the Green function is linear, reflecting the fact that the signal field is considered small. Finally, the expressions for the functions $\alpha(z, t)$ and $\beta(z, t)$ are given in terms of the sampling field $E_S(z, t)$ and the induced relative plasma density $\rho(z, t)$:

$$\alpha(z, t) = -\frac{N_0 I_p}{2c\epsilon_0 E_S^2(z, t)} \frac{\partial \rho(z, t)}{\partial t}, \quad (3)$$

$$\beta(z, t) = -\frac{\chi_3}{2c} E_S^2(z, t), \quad (4)$$

$$\gamma(z, t) = -\frac{N_0 e^2}{2c \epsilon_0 m_e} \rho(z, t). \quad (5)$$

Here, N_0 is the concentration of atoms/molecules, I_p is the bandgap, c is the vacuum light velocity, ϵ_0 is the vacuum permittivity, χ_3 is the third-order susceptibility which describes the mixing of two photons of the pump field and, one photon of the signal, m_e is the (effective) electron mass.

2 Distribution of plasma density with the propagation length

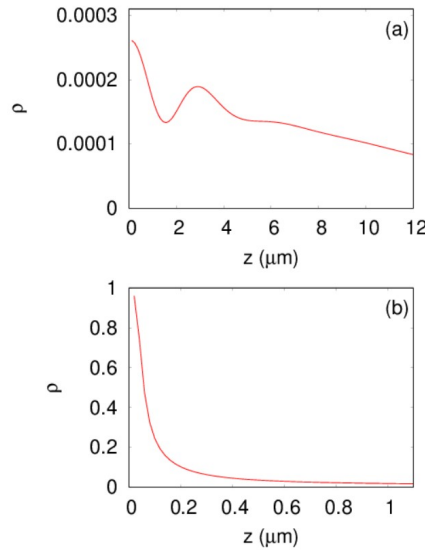


Fig. 1 Dependence of the plasma density ρ after the sampling pulse on the propagation coordinate, for the sampling pulse field strength of 1.54 V/\AA (a) and 5 V/\AA (b).

In Fig. 1, we show the distribution of the plasma in the sample, according to the simulations. One can see that even for the field of 1.54 V/\AA , we predict that plasma is concentrated near the front surface of the sample. The reason for this is sampling pulse absorption due to photoionization (pump depletion). The concentration of carriers near the front surface becomes even more pronounced for higher intensities of the sampling pulse, as shown in Fig. 1(b). Therefore for high intensities, plasma-related processes are concentrated in the very thin layer at the entrance surface, indicating that it would be useful to consider a very thin free-standing film as a nonlinear medium.

3 Separation of the IS and DS terms in the nonlinear response

To separate IS and DS terms, we formally split the real-valued electric field $E(t)$ into positive-frequency and negative-frequency complex-valued time-dependent components as

$$E^\pm(t) = \hat{F}^{-1}\{[0.5 \pm 0.5H(\omega)]\hat{F}[E(t)]\}, \quad (6)$$

where \hat{F} is the Fourier transform and \hat{F}^{-1} is its inversion, while $H(\omega)$ is the Heaviside function. After some straightforward algebraic manipulations, we show that the corresponding terms in the polarization $P_{NL}(t) = P_{NL,IS}(t) + P_{NL,DS}(t)$ look like

$$P_{NL,IS}(t) = 0.75\epsilon_0\chi_3E(t)^3 + 0.75\epsilon_0\chi_3C(t)^3 \quad (7)$$

and

$$P_{NL,DS}(t) = 0.25\epsilon_0\chi_3E(t)^3 - 0.75\epsilon_0\chi_3C(t)^3, \quad (8)$$

where we define an auxiliary real-valued electric field $C(t) = \hat{F}^{-1}\{[-1+2H(\omega)]\hat{F}[E(t)]\}$.

4 Optical system

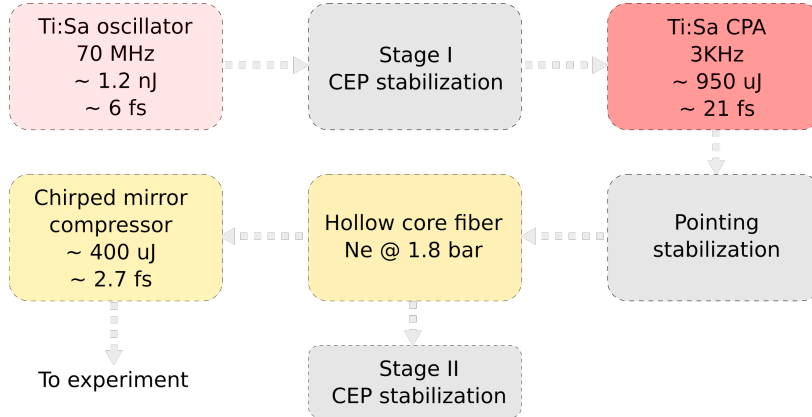


Fig. 2 Diagram of the experimental beam-line.

Fig. 2 shows a schematic of the laser beamline[1, 2] used for the experiments. Ti:sapphire oscillator (Rainbow 2, Spectra Physics) provides an octave-spanning bandwidth with about ~ 750 nm central wavelength. The output from the oscillator is guided through the "stage I" CEP stabilization module based on the feed-forward scheme[2]. CEP stable pulses are further amplified within a 9-pass cryo-cooled

Ti:sapphire chirped-pulse amplifier at a repetition rate of 3 kHz, and temporally compressed using a transmission grating-based compressor yielding ~ 21 fs pulses with ~ 2.5 W output power. The amplified pulses are further spectrally broadened in a hollow-core fiber (HCF), filled with 1.8 bar of neon gas resulting in a spectral broadening to a bandwidth of about 450 - 1000 nm. The chirped mirror compressor consisting of 3 pairs of chirped mirrors in combination with about 6 mm of fused silica glass and 50 cm of air is then used to compress the broadened spectrum to about ~ 2.7 fs (FWHM) duration pulse[3]. The compressed pulses are guided to the experimental setup. The small fraction of spectrally broadened light is reflected from the Brewster window of the hollow core fiber sealing and guided to a 'Stage II CEP stabilization'. The Stage II stabilization is based on f-to-2f technique [4].

5 Data acquisition

The signal from GHOST detection was a current generated by a photodiode (ALPHALAS). This current was first converted into voltage with further amplification by a transimpedance amplifier (DLPCA-200, FEMTO Messtechnik). The amplified voltage signal was connected to a dual-phase lock-in amplifier (SR-830, Stanford Research Systems), triggered by an electrical signal synchronized with half of the repetition rate of the laser.

The measured signal from the lock-in amplifier was read by software on a computer via GPIB interface (National Instruments).

6 Sample medium characterization

In order to precisely determine the spectral response, the propagation effects within a nonlinear medium should be considered. For this, the precise thickness of the medium must be known. The thickness can be determined with a conventional spectrometer and a broadband light source. An optical pulse gets reflected at both surfaces of a sample. After an even number of reflections, light travels in the same direction as the incident pulse, but it is delayed due to a longer propagation through the medium. Multiple pulses in the time domain will result in spectral fringes, which can be measured with a spectrometer. The total transmission of a medium, which takes into account reflections at the surfaces, is given by

$$T(n, \omega, d) = \frac{1}{\cos\left(\frac{\omega}{c}nd\right) - \frac{i}{2}\left(n + \frac{1}{n}\right)\sin\left(\frac{\omega}{c}nd\right)}, \quad (9)$$

where T is the intensity transmission, n is the real-valued refractive index at a frequency ω , c is the vacuum speed of light, and d is the sample thickness.

To precisely measure the thickness of z -cut α -quartz sample, the intensity spectrum of a broadband pulse (section 4) was measured with and without the sample (Fig. 3). The spacing of fringes was then modeled with Eq. (9), where we evaluated

the frequency-dependent refractive index using the Sellmeier equation[5]. The calculated sample thickness is the one that provides the best agreement of fringe positions in the experiment.

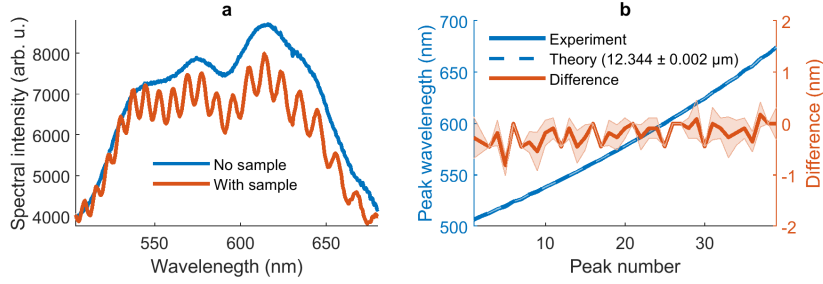


Fig. 3 Measured change of spectral intensities with a z-cut α -quartz sample (a). Positions of spectral fringes allow extracting a sample thickness for the sample (b).

The z-cut α -quartz crystal sample was provided by MTI Corporation, and its thickness was further reduced by polishing.

7 Experimental setup

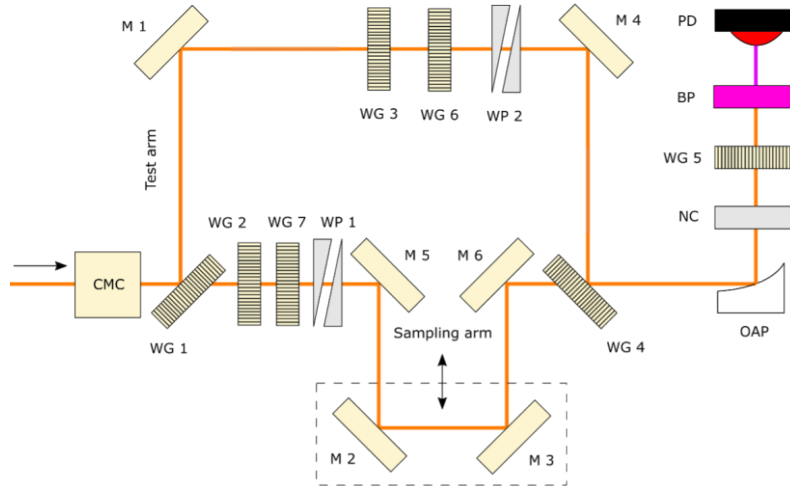


Fig. 4 Optical setup. WG – wire-grid polarizer, WP – wedge pair, M – protected silver mirror, NC – nonlinear crystal, BP – bandpass filter, PD – photodiode, CMC – chirped mirror compressor.

The experimental setup is shown in Fig. 4. After the chirped mirror compressor (CMC), the pulse is split into two optical arms (sampling and test). The test pulse

is transmitted through the set of wire-grid polarizers (WG 3, WG 6) for adjusting the pulse energy. The wedge pair (WP 2) is used for the fine-tuning the compression of the test pulse. After setting the test pulse energy and compression, the pulse is recombined with the sampling arm by the wire-grid polarizer WG 4.

The sampling pulse undergoes a similar procedure as the test pulse where the wire-grid polarizers WG 2 and WG 7 are used to set the pulse energy while the wedge pair WP 1 is used for fine-tuning the pulse compression. The delay line consisting of M 2 and M 3 protected silver mirrors placed on a linear closed-loop piezo stage (PX 200, Piezosystems Jena) for adjusting the delay between sampling and test pulses.

After recombination of the sampling and test pulses with the wire grid, both cross-polarized pulses are focused with an off-axis protected silver parabolic mirror (OAP) on the nonlinear crystal (NC). The nonlinear crystal is a z-cut α -quartz crystal of 12 μm thickness. The emerging local oscillator and a signal are chosen [6] by means of the wire-grid polarizer WG 5, while the detection frequency is defined by the narrow bandpass filter centred at about 0.845 PHz. The interfering local oscillator and the signal are incident on a photodiode.

8 The spectral response of the photodiode and bandpass filter

To get a more accurate experimental spectral response of detection, as well as to perform simulations close to experimental conditions, we took into account the spectral sensitivity of the photodiode (ALPHALAS GmbH) and the transmission of the bandpass filter (Thorlabs) (Fig. 5). ALPHALAS GmbH provided the spectral sensitivity of the photodiode.

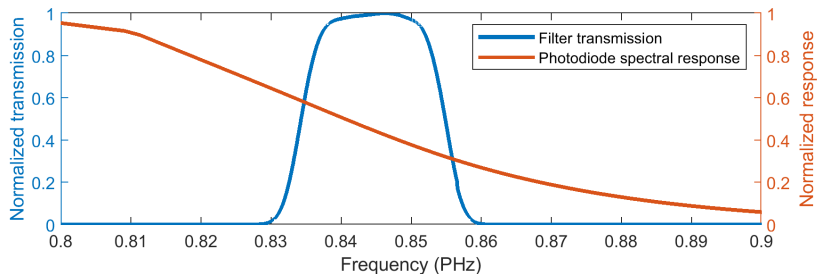


Fig. 5 The spectral response of the photo-diode and the measured transmission of the bandpass filter used in the experiment.

References

- [1] Cavaliere, A.L., Goulielmakis, E., Horvath, B., Helml, W., Schultze, M., Fieß, M., Pervak, V., Veisz, L., Yakovlev, V.S., Uiberacker, M., Apolonski, A., Krausz, F., Kienberger, R.: Intense 1.5-cycle near infrared laser waveforms and their use for

- the generation of ultra-broadband soft-x-ray harmonic continua. *New Journal of Physics* **9**(7), 242–242 (2007) <https://doi.org/10.1088/1367-2630/9/7/242>
- [2] Paasch-Colberg, T.: Ultrafast, optical-field-induced currents in solid-state materials. PhD thesis, Technische Universität München (2014)
- [3] Sederberg, S., Zimin, D., Keiber, S., Siegrist, F., Wismer, M.S., Yakovlev, V.S., Floss, I., Lemell, C., Burgdörfer, J., Schultze, M., Krausz, F., Karpowicz, N.: Attosecond optoelectronic field measurement in solids. *Nature Communications* **11**(1), 430 (2020) <https://doi.org/10.1038/s41467-019-14268-x>
- [4] Schultze, M.: Attosecond real time observation of ionization and electron-electron interactions. PhD thesis, Ludwig Maximilian University of Munich (2008)
- [5] Ghosh, G.: Dispersion-equation coefficients for the refractive index and birefringence of calcite and quartz crystals. *Optics Communications* **163**(1-3), 95–102 (1999) [https://doi.org/10.1016/s0030-4018\(99\)00091-7](https://doi.org/10.1016/s0030-4018(99)00091-7)
- [6] Zimin, D.A., Yakovlev, V.S., Karpowicz, N.: Ultra-broadband all-optical sampling of optical waveforms. *Science Advances* **8**(51), 1029 (2022) <https://doi.org/10.1126/sciadv.ade1029> <https://www.science.org/doi/pdf/10.1126/sciadv.ade1029>